Structural analyses of *Trichomonas vaginalis* pyrophosphate-dependent phosphofructokinase (*Tv*PPi-PFK)

Avery Chiu[a], Lijun Liu[bc], Steve Seibold[bc], Kevin Battaile[d], Justin Craig[a], Elizabeth Harmon[a], Sandhya Subramanian[ef], Graham Chakafana[g], Julie Early[ef], Lisabeth Cron[ef], Bart Staker[ef], Peter J. Myler[ef], Scott Lovell[bf], Wesley C. Van Voorhis[af], Oluwatoyin A. Asojo[hf]

[a]Center for Emerging and Re-emerging Infectious Diseases, University of Washington
SLU Campus E-606, MS 358061, 750 Republican St., Rm E-606, Seattle WA 98109-4766 USA

[b] Protein Structure and X-ray Crystallography Laboratory, 2034 Becker Drive Lawrence, KS 66047

[d]NYX, New York Structural Biology Center, Upton, NY 11973, USA

[e]Center for Global Infectious Disease Research, Seattle Children's Research Institute, 307 Westlake Avenue, North Suite 500, Seattle, Washington, 98109, United States

[f]Seattle Structural Genomics Center for Infectious Diseases, Seattle, Washington, United States

[g]Department of Chemistry and Biochemistry, Hampton University, Hampton VA, USA

[h]Dartmouth Cancer Center, One Medical Center Drive, Lebanon, NH, 03756, USA

*Correspondence email: oluwatoyin.a.asojo@dartmouth.edu
Avery Chiu achiu5@uw.edu 0009-0002-6681-1888
Lijun Liu liulj@ku.edu 0000-0003-0514-281X
Steve Seibold stevesei@ku.edu 0000-0001-8297-229X
Kevin Battaile kbattaile@bnl.gov 0000-0003-0833-3259
Justin Craig craigj3@uw.edu
Elizabeth Harmon ekharmon@uw.edu, 0000-0002-0017-2705
Sandhya Subramanian, Sandhya.Subramanian@seattlechildrens.org
Graham Chakafana, Graham.Chakafana@hamptonu.edu 0009-0000-1316-116X
Julie Early julie.early@seattlechildrens.org
Lisabeth Cron Lisabeth.Cron@seattlechildrens.org
Bart Staker Bart.staker@seattlechildrens.org
Peter J. Myler Peter.Myler@seattlechildrens.org
Scott Lovell swlovell@ku.edu 0000-0002-3215-4472
Wesley C. Van Voorhis wesley@uw.edu 0000-0001-6141-2015
Oluwatoyin A. Asojo oluwatoyin.a.asojo@dartmouth.edu 0000-0002-4043-2700

Synopsis The production, crystallization, and three crystal structures of a pyrophosphate-dependent phosphofructokinase from *Trichomonas vaginalis* (*Tv*PPi-PFK) reveal ATP binding and structural similarity to both ATP-dependent and pyrophosphate-dependent phosphofructokinases. *Tv*PPi-PFK dephosphorylates ATP and has a novel ATP-PFK-like ATP-binding cavity.

Abstract

Trichomonas vaginalis causes trichomoniasis, the most common non-viral sexually transmitted disease in humans. *T. vaginalis* pyrophosphate-dependent phosphofructokinase (*Tv*PPi-PFK) is a putative target for rational, structure-based drug discovery, given its absence in mammals and its importance for parasite survival. *Tv*PPi-PFK is a cytosolic enzyme that catalyzes the phosphorylation of fructose-6-phosphate using pyrophosphate (PPi) as the phosphoryl donor. This reversible reaction, catalyzed by *Tv*PPi-PFK, is the first committed step in glycolysis. Its reverse reaction is vital for gluconeogenesis in *T. vaginalis*. The purification, crystallization, structure determination, and preliminary structure-functional analyses of three crystal structures of *Tv*PPi-PFK are presented. All three structures organize as tetramers with the conserved motifs essential for pyrophosphate binding and PPi-PFK catalytic activity. Comparative analysis with structural neighbors from other organisms demonstrated that despite sharing <29% sequence identity, *Tv*PPi-PFK's protomer shares overall topology with both PPi- and ATP-dependent PFKs. Mass photometry confirmed that *Tv*PPi-PFK formed tetramers under near-physiological conditions. Unexpectedly, *Tv*PPi-PFK crystals dephosphorylate ATP to AMP during soaking. In all three structures, either ATP or AMP is bound at the enzyme's dimer interface, typical of ATP-PFKs, but a novel finding for PPi-PFKs. Furthermore, a sugar phosphate binding site was observed in proximity to the ATP-binding site. Thus, the three reported *Tv*PPi-PFK structures validate its established PPi-dependent activity while revealing previously unreported ATP and sugar phosphate binding. This study also lays a foundation for future research into putative ATP-dependent activity of *Tv*PPi-PFK and for evaluating known phosphofructokinase inhibitors as potential therapeutics for trichomoniasis. These findings expand our understanding of PFK superfamily diversity and support the continued exploration of *Tv*PPi-PFK as a drug target for trichomoniasis.

Keywords: trichomoniasis, Seattle Structural Genomics Center for Infectious Disease (SSGCID), sexually transmitted diseases, Cancer, *Trichomonas vaginalis*, ATP

1. Introduction

The unicellular parasitic protozoan *Trichomonas vaginalis* (*T. vaginalis*) causes ~156 million new annual cases of trichomoniasis, the most prevalent non-viral sexually transmitted disease globally [1-3]. Approximately 3.7 million people in the USA have trichomoniasis, exceeding both chlamydia and gonorrhea combined and population studies show that the highest incidence is among incarcerated women [2]. *T. vaginalis* exclusively infects humans, and trichomoniasis leads to higher rates of HIV, infertility, pre-term birth, HPV, cervical, and prostate cancer [4-6]. *T. vaginalis* is anaerobic, thriving in

the urethra, vagina, and vulva, and is readily spread by asymptomatic people with ~1.1 million new infections annually in the USA[7-9]. Trichomoniasis is most often treated with oral antibiotics: a single dose of 2 g of tinidazole, a 7-day course of twice-daily 500mg metronidazole, or a single or 5-day course of secnidazole[10]. Drug resistance to metronidazole was identified over 60 years ago [11]. Current treatments often fail if alcohol is consumed, and reinfection is common if partners are not treated, and allergic reactions may affect compliance [10]. There is therefore a need to identify alternative new therapeutics and therapeutic targets for trichomoniasis.

T. vaginalis is a priority infectious disease for structural studies by the Seattle Structural Genomics Center for Infectious Disease (SSGCID) because of its clinical significance. SSGCID studies include the determination of the structures of potential new *T. vaginalis* therapeutic targets and vital metabolic enzymes such as pyrophosphate-fructose 6-phosphate 1-phosphotransferase 1 (PFP-1). PFP-1, also referred to as pyrophosphate-dependent phosphofructokinase (PPi-PFK), catalyzes the first committing step in glycolysis, the phosphorylation of fructose 6-phosphate. PPi-PFK uses pyrophosphate (PPi) as the phosphoryl donor to catalyze the synthesis of fructose 1,6-bisphosphate and inorganic phosphate (Table 1). Since the reaction is reversible, PPi-PFK functions in both glycolysis and gluconeogenesis. This is a deviation from the otherwise well-known reaction in glycolysis catalyzed by ATP-PFK in which adenosine triphosphate (ATP) is used as the phosphoryl donor instead of PPi (Table 1)[12-14].

T. vaginalis has both PPi-PFK and ATP-PFK enzymes[12-14]. *Tv*PPi-PFK is a cytosolic enzyme responsible for most of *T. vaginalis'* glycolytic flux and energetic needs[14]. *T. vaginalis* has four ATP-PFK enzymes, which have less than 2% of the activity of the PPi-PFK[13, 14]. Furthermore, all four *Tv*ATP-PFK are localized in the hydrogenosomes, which are double membrane organelles that *T. vaginalis* possesses instead of mitochondria[12-14]. To facilitate future therapeutic discovery, we present the purification, crystallization, and structural and functional analyses of *Tv*PPi-PFK.

Table 1. Comparison of ATP-PFK and PPi-PFK

Enzyme	**ATP-PFK (EC 2.7.1.11)**	**PPi-PFK (EC 2.7.1.90)**
Phosphate source	ATP	PPi
Reaction	ATP + F6P → ADP + F1,6BP	PPi + F6P ⇌ Pi + F1,6BP
Thermodynamics	Irreversible in vivo	Near-equilibrium, reversible
Regulation	Major glycolytic regulatory point	PPi homeostasis, glycolysis etc
Typical organisms	Animals, fungi, many bacteria	Plants, protists, archaea, anaerobic parasites

2. Materials and methods

2.1. Macromolecule production

*Tv*PPi-PFK was cloned, expressed, and purified using standard methods developed by the SSGCID[15-17]. The full-length gene for pyrophosphate-fructose 6-phosphate 1-phosphotransferase 1 (PFP-1) from *Trichomonas vaginalis ATCC PRA-98 / G3* (Uniprot A2DXT4) encoding amino acids 1-426 was PCR-amplified from gDNA using the primers shown in Table 2, cloned into the BG1861 and then the plasmid DNA was transformed into chemically competent *Escherichia coli* BL21(DE3) cells. After

testing for expression, 2L of culture was grown using auto-induction media[18] in a LEX Bioreactor (Epiphyte Three) as described previously[17]. The expression clone HepyC.00487.a.B1.GE40934 is available at https://www.ssgcid.org/available-materials/expression-clones/.

N-terminal hexa-histidine tagged *Tv*PPi-PFK was purified using the standardized previously described two-step protocol of an immobilized metal (Ni^{2+}) affinity chromatography (IMAC) step followed by size-exclusion chromatography (SEC) on an AKTApurifier 10 (GE Healthcare) using automated IMAC and SEC programs[17]. Briefly, thawed bacterial pellets (25 g) were lysed by sonication in 200 ml lysis buffer (25 mM HEPES pH 7.0, 500 mM NaCl, 5% (v/v) glycerol, 0.5% (w/v) CHAPS, 30 mM imidazole, 10 mM $MgCl_2$, 400 µg/ml AEBSF and 0.025% (w/v) sodium azide. After sonication, the crude lysate was incubated with 20 ml of benzonase (25 units/ml) at room temperature for 45 min with mixing. After clarifying the lysate by centrifugation (~10,000 g for 1 hour using a Sorvall centrifuge, Thermo Scientific), the clarified supernatant was passed over a Ni-NTA HisTrap FF 5 ml column (GE Healthcare), which was pre-equilibrated with wash buffer (25 mM HEPES pH 7.0, 500 mM NaCl, 5% (v/v) glycerol, 30 mM imidazole). The column was washed with 20 column volumes (CV) of wash buffer and eluted with elution buffer (20 mM HEPES, pH 7.0, 500 mM NaCl, 5% (v/v) glycerol, 500 mM imidazole) over a 7CV linear gradient. Peak fractions were pooled, concentrated to ~5 ml for SEC. The ~5ml protein sample was loaded onto a Superdex 75 26/60 column (GE Biosciences) attached to an ÄKTA Prime-plus FPLC system (GE Biosciences) that was equilibrated with SEC buffer (20 mM HEPES, pH 7.0, 300 mM NaCl, 5% glycerol, and 1 mM TCEP). The peak fractions were collected and assessed for purity by SDS-PAGE. *Tv*PPi-PFK eluted as a single, symmetrical, monodisperse peak, accounting for >90% of the protein product of molecular mass ~46 kDa (close to the theoretical molecular weight 47.6 kDa of recombinant Histagged *Tv*PPi-PFK) as assessed by molecular weight standards. The peak fraction was pooled and concentrated to ~25 mg/ml with an Amicon purification system (Millipore). 110 µl aliquots of recombinant *Tv*PPi-PFK were flash-frozen in liquid nitrogen and stored at -80°C until used. Recombinant *Tv*PPi-PFK is available for request online at www.ssgcid.org/available-materials/ssgcid-proteins/.

Table 2 Macromolecule production information

Source organism	*Trichomonas vaginalis* ATCC PRA-98 / G3
DNA source	ATCC Representative, ATCC
Forward primer	5'CTCACCACCACCACCACCATATGAGCACTGAAGCTCCTGTTCT3'
Reverse primer	5'ATCCTATCTTACTCACTTATTCGACGACAACATCTGTAAGGTG3'
Expression vector	BG1861, Histag N-term tag
Expression host	*Escherichia coli* BL21(DE3)
Complete amino acid sequence of the construct produced. The N-terminal hexa-histidine residues are highlighted in yellow.	**MAHHHHHH**MSTEAPVLGILCGGGPAPGLNGVIAGATLYALRLGWKVIGFM EGFKYLCTGDVDVVKAHTIDLTYDIVSRIHFQGGTIIQTSRANPRKSPELQEN VRKCLRALKVRYFLTIGGDDTASSAVSVASGMNGNEISVISCPKTIDNDLPLP ADQSTFGFHTARSLGMEIIRNLMVDSKSAPRWFLVEAMGRSAGHLALGMAE ASGAHLCLIPEEFKQDEIEFEDVVELVEATILKRLAYGKNYGVCVLAEGLVS KMSKKALYKLFGNREPPTDPHGHILLDDAELARSLSEELLKRLGNLGIRITPK KIGYELRCADPVAFDAVYTRELGYGAIDAFLNGHSAALIVRENGQVKPVQFK DLLDPATGRVRTRLVDVTSQSFKVARVYMWRMSKKDYENKDLVARVAAA GKMTPEAFTEKFAHLTDVVVE

2.2. Crystallization

All crystallization experiments were conducted using an NT8 drop-setting robot (Formulatrix Inc.) and UVXPO MRC (Molecular Dimensions) sitting-drop vapor diffusion plates at 17 °C. 100 nL of protein and 100 nL of crystallization solution were dispensed and equilibrated against 50 µL of the latter. Three crystal forms of *Tv*PPi-PFK are reported, and all crystals were grown by sitting-drop vapor diffusion using the Morpheus[19] (Molecular Dimensions) crystallization screen (Table 3).

Table 3 Crystallization

Accession code	9MDT (pdb_00009mdt)	9MF6 (pdb_00009mf6)	9MED (pdb_00009med)
Method	Vapor diffusion, sitting drop	Vapor diffusion, sitting drop	Vapor diffusion, sitting drop
Plate type	Plate Liu-S-143 AB34	Plate Liu-S-143 AB34	Plate Liu-S-143 AB34
Temperature	291K	291K	291K
Protein concentration	25 mg mL^{-1}	25 mg mL^{-1}	25 mg mL^{-1}
Buffer composition of protein solution	20 mM HEPES, pH 7.0, 300 mM NaCl, 5% glycerol, and 1 mM TCEP	20 mM HEPES, pH 7.0, 300 mM NaCl, 5% glycerol, and 1 mM TCEP	20 mM HEPES, pH 7.0, 300 mM NaCl, 5% glycerol, and 1 mM TCEP
Composition of reservoir solution	Morpheus A4: 12.5%(v/v) MPD, 12.5%(v/v) PEG 1000, 12.5% (w/v) PEG 3350, 100 mM Imidazole/MES, pH 6.5, 30 mM $MgCl_2$ and 30 mM $CaCl_2$	Morpheus A4: 12.5%(v/v) MPD, 12.5%(v/v) PEG 1000, 12.5% (w/v) PEG 3350, 100 mM Imidazole/MES, pH 6.5, 30 mM $MgCl_2$ and 30 mM $CaCl_2$	Morpheus A4: 12.5%(v/v) MPD, 12.5%(v/v) PEG 1000, 12.5% (w/v) PEG 3350, 100 mM Imidazole/MES, pH 6.5, 30 mM $MgCl_2$ and 30 mM $CaCl_2$
Soaking of crystal in reservoir solution containing	5 mM ATP and 5 mM pyrophosphate (PPi)	2 mM ADP and α-D-Ribose 5-phosphate (R5P)	2 mM AMP, β-D-Glucose-6-phosphate (G6P)
Volume and ratio of drop	0.2 µl : 0.2 µl	0.2 µl : 0.2 µl	0.2 µl : 0.2 µl
Volume of reservoir	40 µl	40 µl	40 µl

2.3. Data collection and processing

All datasets were collected at 100 K on a DECTRIS EIGER2 XE 9M detector at NSLS-II BEAMLINE 19-ID at Brookhaven National Laboratory (Table 4). Data were integrated with XDS and reduced with XSCALE [20]. Raw X-ray diffraction images are stored at the Integrated Resource for Reproducibility in Macromolecular Crystallography at https://www.proteindiffraction.org.

Table 4 Data collection and processing (Values for the outer shell are given in parentheses).

Accession Codes	9MDT (pdb_00009mdt)	9MF6 (pdb_00009mf6)	9MED (pdb_00009med)
Diffraction source	NSLS-II beamline 19-ID	NSLS-II beamline 19-ID	NSLS-II beamline 19-ID
Wavelength (Å)	0.9786	0.9786	0.9786
Temperature (K)	100	100	100
Detector	Dectris EIGER2 XE 9M pixel	Dectris EIGER2 XE 9M pixel	Dectris EIGER2 XE 9M pixel
Space group	*P*4□*2*□2	$P4_32_12$	$P4_32_12$
a, b, c (Å)	87.11, 87.11, 478.24	86.96, 86.96, 473.87	86.88, 86.88, 475.98
α, β, γ (°)	90, 90, 90	90, 90, 90	90, 90, 90
Resolution range (Å)	49.29–2.16 (2.22–2.16)	48.96–2.65 (2.73–2.65)	49.09-2.62 (2.69-2.62)
Total number of reflections	2652128 (180151)	690768 (60604)	732317 (56331)
Completeness	100.0 (100.0)	100.0 (100.0)	100.0 (100.0)
Redundancy	26.3 (24.7)	12.6 (13.7)	12.9 (13.8)
$\langle I/\sigma(I)\rangle$	21.8 (1.7)	15.1 (1.8)	21.8 (2.0)
$R_{r.i.m.}$	0.133 (2.164)	0.100 (1.658)	0.103 (1.437)
$R_{p.i.m.}$	0.026 (0.433)	0.028 (0.445)	0.028 (0.385)

2.4. Structure solution and refinement

The three structures were determined by molecular replacement with Phaser (McCoy et al., 2007) from the CCP4 suite of programs[21-24]. The molecular replacement search model pdb entry 9DQM. The structures were refined by iterative model building with COOT[25] and PHENIX[26, 27]. Structure quality was checked with MolProbity[28]. Data-reduction and refinement statistics are shown in Table 5. Coordinates and structure factors have been deposited with the Worldwide PDB (wwPDB) under the accession codes 9MDT (pdb_00009mdt), 9MF6 (pdb_00009mf6), and 9MED (pdb_00009med).

Table 5 Structure solution and refinement

Accession codes	9MDT (pdb_00009mdt)	9MF6 (pdb_00009mf6)	9MED (pdb_00009med)
Components			
Protein	4 *Tv*PPi-PFK	4 *Tv*PPi-PFK	4 *Tv*PPi-PFK
Ligands	3ATP, 1AMP, 4PPi (PPV), $8PO_4^{3-}$, $7Cl^-$	4R5P (HSX), 4AMP, $MgPPi^{2-}$ (1PPV and 1Mg)	$1MgPPi^{2-}$ (1PPV, 1Mg), $1Cl^-$, 4AMP, 2G6P (BG6), $9PO_4^{3-}$
Resolution range (Å)	49.29–2.16 (2.22–2.16)	48.96–2.65 (2.73–2.65)	49.09-2.62 (2.69-2.62)
Number of reflections, working set			
Number of reflections, test set	4984 (150)	2628 (149)	2768 (141)
Final R_{cryst}	0.202 (0.312)	0.208 (0.308)	0.192 (0.276)
Final R_{free}	0.229 (0.336)	0.263 (0.353)	0.234 (0.324)
Number of non-H atoms			
Protein	12871	12432	12863
Ion	47	1	47
Ligand	152	157	133
Water	173	28	16
Total	13243	12618	13059
R.m.s. deviations			
Bonds (Å)	0.005	0.003	0.003
Angles (°)	0.603	0.512	0.649
Average *B* factors ($Å^2$)			
Protein	62.8	90.2	81.9
Ion	77.6	99.5	104.1
Ligand	82.0	85.8	86.9
Water	47.7	62.8	53.6
Ramachandran plot			
Most favored (%)	95	96	96
Allowed (%)	5	4	4

2.5. Mass Photometry

Mass photometry measures the molecular weight and relative abundance of proteins in a sample with light scattering for an analytical range of 40 kDa - 5 MDa [29, 30]. Standard methods established by Dr. Lisa Tuttle (University of Washington) were followed. 24x50 mm glass coverslips were cleaned with isopropanol and dried with nitrogen gas. The TwoMP Mass Photometer instrument (Refeyen Ltd,

Oxford, UK) was calibrated with 50 nM β-amylase. 10 μl of buffer solution SEC (20 mM HEPES, 300 mM NaCl, 5% glycerol, and 1 mM TCEP) was measured in sample gasket wells, followed by 10 μl of the ∼50 nM protein samples at Room Temperature. The first condition was recombinant *Tv*PPi-PFK in SEC buffer. The second condition is *Tv*PPi-PFK in SEC buffer with 5 mM ATP, 5 mM PPi, and 5 mM $MgCl_2$. Mass histograms were collected with the DiscoverMP analysis software and analyzed with single Gaussian fits in IGOR-Pro v.8 (Wavemetrics, Lake Oswego, OR).

3. Results and discussion

Crystallization results

The crystallized *Tv*PPi-PFK protein included 8 additional vector-derived N-terminus amino acid residues, including a hexahistidine tag (Table 2). These vector-derived N-terminal residues are disordered and were not modeled in the three structures reported in this manuscript (pdb entries 9MDT, 9MED, and 9MF6). Most mature polypeptide main-chain and side-chain residues were ordered and built for all three structures. All three crystal structures of *Tv*PPi-PFK contain a homotetramer in the asymmetric unit (Table 5). The three *Tv*PPi-PFK structures are modelled as complexes with inorganic pyrophosphate (PPi), adenosine triphosphate (ATP), adenosine monophosphate (AMP), phosphate (PO_4^{3-}), α-D-Ribose 5-phosphate (R5P), or β-D-glucose 6-phosphate (G6P), magnesium, and chloride ions (Table 5). Recombinant *Tv*PPi-PFK is expressed in media that contains phosphate, magnesium, and chloride ions[18]. The crystallization solution also contains magnesium and chloride ions. No exogenous PPi, ATP, ADP, or AMP is present in the production, purification, or crystallization solutions prior to the soaking experiments.

Overall structure and oligomerization

Each polypeptide chain of *Tv*PPi-PFK adopts the prototypical topology of a PPi-PFK, with the pyrophosphate-binding site sitting between the N-terminal and C-terminal domains (Figure 1a). PROMOTIF analysis reveals that each *Tv*PPi-PFK protomer's secondary structure is ~15% strand, ~41% alpha helix, 7% 3-10 helix, and 37% loops/other. Each *Tv*PPi-PFK chain assembles into 2 beta-sheets (a 7-stranded mixed sheet and a 4-stranded parallel sheet). 3 beta-alpha-beta motifs, and 2 beta hairpins. The asymmetric unit contains four copies of the polypeptide (chains A-D), forming a dimer of two tightly packed dimers (Figures 1b-f). All the polypeptide chains are very similar, with an rmsd of ~0.2 Å when superimposing all main-chain atoms. In the three *Tv*PPi-PFK structures discussed in this manuscript, the asymmetric unit contains a homotetramer with an estimated molecular weight of ~193kDa, suggestive of the canonical tetrameric PPi-PFK fold. The homotetramers of all three reported structures are very similar (rmsd of ~0.3Å for the alignment of all main chain atoms), which is comparable to the (Figures 1b & 1c). The homotetramer has four large

dimer interfaces (Figures 1d-f). The larger dimer between chains A and chain D (equivalent to chains C and B) has a buried surface area of ~2230 $Å^2$. This is approximately double the ~1270 $Å^2$ buried surface area of the smaller dimer interface between chains A and chain C (equivalent to chains D and B).

*Tv*PPi-PFK is predicted to be a biological tetramer based on Proteins, Interfaces, Structures, and Assemblies (PDBePISA) analysis[31]. This is consistent with purified *Tv*PPi-PFK isolated from *T. vaginalis,* which assembles as a tetramer in solution[32]. SEC analysis using molecular weight standards suggests that recombinant *Tv*PPi-PFK purifies as a monomer; however, mass photometry experiments reveal that recombinant *Tv*PPi-PFK is mainly tetrameric with smaller monomer and dimer peaks (Figure 2a). Furthermore, the addition of ATP, $MgCl_2$, and pyrophosphate reduces the monomer and dimer peaks to almost neglible level (Figure 2b). Mass photometry data suggest that recombinant *Tv*PPi-PFK is tetrameric in solution under conditions that resemble biological conditions.

Ligand binding and PPi-PFK motifs

In one *Tv*PPi-PFK structure (pdb entry 9MDT), all PPi binding sites for all 4 polypeptide chains are occupied by PPi. In the other two structures (PDB entries 9MED and 9MF6), one PPi-binding site is occupied with $MgPPi^{2-}$ (modelled as PPi (PPV) and 1Mg). While the other sites are occupied by phosphate ions. In all three structures, as expected, PPi binds in the substrate-binding cavity and forms close interactions with Gly14, Gly15, Arg83, Gly113, Thr116, Asp115, and Lys139 (Figures 3a-c). The residues involved in PPi binding are key classical pyrophosphate-dependent phosphofructokinase residues and motifs. *Tv*PPi-PFK has the canonical PPi-PFK pyrophosphate binding glycine (G15). The substrate-binding site contains the prototypical GGDD motif that ensures PPi specificity. The GGDD motif includes D114, which is important for Mg^{2+} binding, and D115, which is important for catalytic activity and stabilizes the transition state when PPi is the phosphoryl donor. *Tv*PPi-PFK's pyrophosphate-binding site with and without PPi is very similar and the amino acids superpose well (Figure 3d).

A second key conserved PPi-PFK motif is the "KTID" substrate binding site-motif, which contains the catalytic lysine (Lys139). As expected, Lys139 is positioned to stabilize the transition state when PPi is the phosphoryl donor, while Asp142 serves as a proton donor. These shifts in *Tv*PPi-PFK's pyrophosphate binding are evident when comparing the structures with and without Mg^{2+}, where the proximity of the divalent cation results in a $MgPPi^{2-}$ complex (Figures 3a-c). Both ATP-PFK and PPi-PFKs require the divalent magnesium cation, the absence of which prevents the formation of fructose 1,6-bisphosphate [33, 34]. In ATP-PFKs, Mg^{2+} and ATP form a $MgATP^{2-}$ complex, while in PPi-PFKs, Mg^{2+} and PPi form a $MgPPi^{2-}$ complex[33, 34]. Mg^{2+} of the $MgPPi^{2-}$ complex in both *Tv*PPi-PFK structures (PDB entries 9MED and 9MF6) interacts with amino acids in the PPi binding

cavity (Asp114, Asp115, and Asp144), while the PPi forms a network of interactions that includes key catalytic residues (Supplementary Figure S.1).

The three reported *Tv*PPi-PFK structures have either ATP or AMP at their dimer interfaces (Figures 1d-1f). While 9MDT has 3 ATP and 1 AMP molecules, both 9MED and 9MF6 contain 4 AMP molecules (Table 5). These molecules interact with the amino acid residues Leu32, Arg33, Tyr65 from one monomer and Lys232, Tyr236, Met385, Trp386 from the second monomer across the dimer interface (Supplementary Figure S2). Trp 386 forms a pi-stacking interaction with the adenine group, while the other residues form pi-stacking, hydrogen bonding, and other interactions with the ATP or AMP (Figure 3e). In one of the reported structures (pdb entry 9MF6), there are 4 R5P (HSX) molecules at the dimer interface (Table 5). These molecules form almost identical interactions across the dimer interface regardless of the monomer pairs. One of the structures (pdb entry 9MED) has two molecules of β-D-glucose 6-phosphate (G6P, B6G) in two of the four dimer interfaces. The LIGPLOT+ analysis[35, 36] reveals that the sugar phosphates (G6P and R5P) bind with a very similar network of interactions to *Tv*PPi-PFK (supplementary Figure S.3). The sugar phosphate-binding sites are occupied by phosphate ions in pdb entry 9MDT, which sit in the same position as the phosphoryl group of the four R5P molecules of pdb entry 9MF6.

Comparison to structural neighbors

ENDScript[37, 38] analysis reveals that the most similar crystal structure to *Tv*PPi-PFK is that of *Candidatus Prometheoarchaeum syntrophicum* PPi-PFK (*CPs*PPi-PFK, pdb entry 9CIR). The next closest is that of the Lyme disease spirochete *Borrelia burgdorferi* PPi-PFK (*Bb*PPi-PFK, pdb entry 1KZH)[39]. These proteins share ~29% sequence identity with *Tv*PPi-PFK. The carboxyl terminal domain of *Tv*PPi-PFK contains the modestly conserved GXXXR motif: GYELR, residues 307-311 in *Tv*PPi-PFK, GYEGR in 1KZH, and GHTMR in *Bb*PPi-PFK (Figure 4). The catalytic conserved substrate-binding "MGR" motif of *Tv*PPi-PFK consists of amino acid residues 186-188. The substrate-binding site also includes the conserved catalytic Glu247 (Figure 4). ENDScript alignment reveals that the N-terminus domains of the proteins are better conserved than their C-terminus domains. The least conserved regions identified by ENDScript alignment are in the C-terminus domains of the three proteins (Figure 4). Compared to the C-terminus domains, the N-terminus domains are well-conserved except for an additional 14 amino acid insertion that extends the alpha helix 5 of *CPs*PPi-PFK (Figure 4, Supplementary Figure S4).

The ENDScript sausage plots and superposed protomers indicate that, despite the low (~29%) sequence similarity, *Tv*PPi-PFK, *CPs*PPi-PFK, and *Bb*PPi-PFK have similar overall topologies (Figures 5a, 5b & 5c). While the protomer of *Tv*PPi-PFK can bind ATP/AMP at its dimer interface, in both the *CPs*PPi-PFK and *Bb*PPi-PFK structures, the corresponding regions appear obscured by both

main chain and side chains (Figures 5b & 5c). This blockage is why typical PPi-PFKs, such as *CPs*PPi-PFK and *Bb*PPi-PFK, are unable to bind ATP. The blockage also ensures substrate-binding specificity of *CPs*PPi-PFK and *Bb*PPi-PFK for PPi.

3D protein structure comparison against the entire RCSB protein database using the DALI server (http://ekhidna2.biocenter.helsinki.fi/dali) was also used to identify the closest structures to *Tv*PPi-PFK[40]. DALI analyses agreed with ENDScript and identified *CPs*PPi-PFK (PDB entries 9CIT, 9CIS) as the closest structures to *Tv*PPi-PFK (Table S.1). Surprisingly, the next closest structure to *Tv*PPi-PFK that was identified was not another PPi-PFK but instead *Trypanosoma brucei* ATP-PFK (*Tb*ATP-PFK).[41] *Tb*ATP-PFK is topologically similar to *Tv*PPi-PFK despite having a larger size and amino and carboxyl termini extension (Figure 5d). Interestingly, allosteric inhibitors of *Tb*ATP-PFK have been identified that also clear *T. brucei* infections in mice[41]. It is unknown if these inhibitors can inhibit *Tv*PPi-PFK activity. The *Tv*PPi-PFK protomer also shares topological similarity with the prototypical bacterial ATP-PFK from *Geobacillus stearothermophilus* (*Gst*ATP-PFK)[42] (Figure 5e). The supplementary DALI alignment tables report RMSD values. While *Tv*PPi-PFK has been confirmed to be a cytosolic enzyme responsible for most of *T. vaginalis'* glycolytic flux and energetic needs[14], its ATP-PFK activity has not been tested and will be the subject of future studies.

Future activity and mutagenesis studies of *Tv*PPi-PFK are also required because *Tv*PPi-PFK crystals are catalytically active and suggest the ability to dephosphorylate ATP to AMP. Evidence supporting this activity includes the observation that crystals soaked with ATP and PPi yielded a crystal structure containing 3ATP, 1AMP, $4PO_4^{3-}$, and 8PPi (pdb entry 9MDT), suggesting the dephosphorylation of 1ATP to AMP by *Tv*PPi-PFK. Furthermore, crystals soaked with ADP and R5P resulted in a structure (pdb entry 9MF6) containing R5P, AMP, and PPi, suggesting dephosphorylation of ADP to AMP. The dephosphorylation of ADP and ATP by *Tv*PPi-PFK crystals was unexpected. Intriguingly, R5P and AMP adopt similar orientations as the fructose 6-phosphate and ATP in the structures of bacterial ATP-PFK superfamily[43], while positioned in proximity to the conserved Asp66 across the dimer interface that can function as the general base catalyst (Figure 3e). Additionally, Arg233 and Arg401 are among the key ATP-binding site residues that may play roles in the dephosphorylation of ADP to AMP (Figure 3f). Our structural analysis thus strongly suggests that *Tv*PPi-PFK binds ATP in a novel ATP-binding site suggestive of ATP-PFK-like activity. A recent review article[43] discussed the complexities and diversities of structure-function relationships of members of the PFK superfamily, and *Tv*PPi-PFK structures add to these complexities by offering new testable hypotheses about *Tv*PPi-PFK's roles in glycolysis as a novel PFK that may utilize both ATP and PPi for glycolysis.

Conclusion

We report three *Tv*PPi-PFK structures, deposited with the Worldwide PDB (wwPDB) under the accession codes 9MDT (pdb_00009mdt), 9MF6 (pdb_00009mf6) and 9MED (pdb_00009med). The three *Tv*PPi-PFK structures validate *Tv*PPi-PFK's previously described PPi-PFK enzymatic activity.[32] Structural analyses reveal novel ATP and sugar phosphate binding at *Tv*PPi-PFK's dimer interface. *Tv*PPi-PFK crystals are catalytically active and can dephosphorylate ATP to AMP. Future mutagenesis and activity studies will determine whether *Tv*PPi-PFK can utilize both ATP and PPi in glycolysis. We also plan to test whether known PFK inhibitors can inhibit *Tv*PPi-PFK activity as a first step towards rational drug repurposing, with *Tv*PPi-PFK as a drug target for *Trichomonas vaginalis.*

Acknowledgements

We thank Dr. Lisa Tuttle for training and guidance with Mass Photometry experiments at The Hans Neurath Biophysics Core of the University of Washington Department of Biochemistry. We thank Abhishek Kancherla for technical assistance. This project has been funded in whole or in part with Federal funds from the National Institute of Allergy and Infectious Diseases, National Institutes of Health, Department of Health and Human Services, under Contract No.: 75N93022C00036. This project is part of a continuing SSGCID collaboration training students in structural science, rational structure-based drug discovery, and scientific communication. This research used resources the NYX beamline 19-ID, supported by the New York Structural Biology Center, at the National Synchrotron Light Source II, a U.S. Department of Energy (DOE) Office of Science User Facility operated for the DOE Office of Science by Brookhaven National Laboratory under Contract No. DE-SC0012704. The NYX detector instrumentation was supported by grant S10OD030394 through the Office of the Director of the National Institutes of Health.

Figure Legends

Figure 1. Overall structure of *Tv*PPi-PFK. (a) A representative protomer of *Tv*PPi-PFK (pdb entry 9MED, chain B, colored in rainbow from blue N- to red C-term) reveals the prototypical two-domain topology of PPi-PFK. Two phosphate molecules sit in the central substrate-binding cavity. Other ligands in the protomer are shown in sticks or spheres. (b) A representative *Tv*PPi-PFK homotetramer with one monomer is shown as a rainbow cartoon (same orientation as figure 1a) while the other three are shown in gray, tan, and blue. (c) Superposed tetramers *Tv*PPi-PFK (pdb entries 9MED, 9MDT, and 9MF6) reveal extensive structural similarity, chain B shown in cyan, chain C in gray, chain A in wheat, and chain D in blue. (d) An alternative view of the superposed tetramers reveals prototypical PPi-PFK homotetramer topology. The homotetramer surfaces plots of *Tv*PPi-PFK reveal large dimer interfaces for (e) 9MED, (f) 9MDT, and (g) 9MF6; some of the bound ligands in the dimer interface are visible from this orientation.

Figure 2. Mass Photometry analysis of recombinant *Tv*PPi-PFK reveals that (a) recombinant *Tv*PPi-PFK forms tetramers, dimers, and monomers in SEC buffer. (b) *Tv*PPi-PFK is primarily a homotetramer under conditions that resemble biological conditions (SEC buffer with $MgCl_2$, PPi, ATP).

Figure 3. Ligand-binding by *Tv*PPi-PFK. Comparison of PPi binding by *Tv*PPi-PFK in the (a) absence and (b) presence of magnesium (c) superpositioning of the states. (d) Comparison of *Tv*PPi-PFK's PPi-binding site with PPi (chain C of pdb entry 9MDT) and without PPi (Chain C of pdb entry MED). (e) ATP binding by *Tv*PPi-PFK is stabilized by residues from the protomer (gray) and from across the dimer interface (green). (f) Alternative view of *Tv*PPi-PFK's putative ATP binding site (pdb entry 4MF6) showing proximity of R5P and AMP and network of amino acid residues within 5 Å. (g) Same view as 3f of *Tv*PPi-PFK's putative ATP binding site, but only showing residues that may be important for putative ATP-PFK activity based on known ATP-PFK structures.

Figure 4. The amino-terminus domain of *Tv*PPi-PFK aligns well with those of its nearest structural neighbors as identified by ENDScript[37, 44]. ENDScript structure-based-sequence alignment reveals the nearest structural neighbors of *Tv*PPi-PFK as Lyme disease spirochete *Borrelia burgdorferi* PPi-PFK (*Bb*PPi-PFK, pdb entry 1KZH)[39] and *Candidatus Prometheoarchaeum syntrophicum* PPi-PFK (*CPs*PPi-PFK, pdb entry 9CIR). Also shown is another *Tv*PPi-PFK structure (pdb entry 9DQM). Identical and conserved residues are highlighted in red and yellow, respectively. The different

secondary structure elements shown are alpha helices (α), 310-helices (η), beta strands (β), and beta turns (TT)[37, 44].

Figure 5. Comparison of *Tv*PPi-PFK to its structural neighbors. (a) Sausage plot calculated by ENDScript. The circumference of the ribbon (sausage) represents relative structural conservation of *Tv*PPi-PFK compared to *CPs*PPi-PFK and *Bb*PPi-PFK. Thinner ribbons represent regions with lower RMSD for alignment. In comparison, thicker ribbons represent higher RMSD for alignment, and the ribbons are colored by sequence conservation, with red indicating identical residues. (b) Same view of representative *Tv*PPi-PFK protomer (pdb entry 9MF6) showing Mg and PPi in the central pyrophosphate binding cavity at the interface of the two domains. Also shown are ligands at the AMP R5P at the dimer interface. (c) Superposed protomers of *Tv*PPi-PFK (pdb entry 9MF6, gray) superposed with *CPs*PPi-PFK (9CIR, green) and *Bb*PPi-PFK (1KZN, wheat) reveal the obstructed ATP-binding region in both *CPs*PPi-PFK and *Bb*PPi-PFK. (d) Superposed protomers of *Tv*PPi-PFK (pdb entry 9MF6, gray) and *Gst*ATP-PFK (4I36, purple) reveal conserved overall topology. (e) Likewise, superposed protomers of *Tv*PPi-PFK (pdb entry 9MF6, gray) and *Tb*ATP-PFK (6QU5, cyan) reveal overall structural similarity. Figures 5a-e are shown in the same orientation.

References

(1) Edwards, T.; Burke, P.; Smalley, H.; Hobbs, G. Trichomonas vaginalis: Clinical relevance, pathogenicity and diagnosis. *Crit Rev Microbiol* **2016**, *42* (3), 406–417. DOI: 10.3109/1040841X.2014.958050.

(2) Satterwhite, C. L.; Torrone, E.; Meites, E.; Dunne, E. F.; Mahajan, R.; Ocfemia, M. C.; Su, J.; Xu, F.; Weinstock, H. Sexually transmitted infections among US women and men: prevalence and incidence estimates, 2008. *Sex Transm Dis* **2013**, *40* (3), 187–193. DOI: 10.1097/OLQ.0b013e318286bb53.

(3) Molgora, B. M.; Mukherjee, S. K.; Baumel-Alterzon, S.; Santiago, F. M.; Muratore, K. A.; Sisk, A. E., Jr.; Mercer, F.; Johnson, P. J. Trichomonas vaginalis adherence phenotypes and extracellular vesicles impact parasite survival in a novel in vivo model of pathogenesis. *PLoS Negl Trop Dis* **2023**, *17* (10), e0011693. DOI: 10.1371/journal.pntd.0011693.

(4) Tsang, S. H.; Peisch, S. F.; Rowan, B.; Markt, S. C.; Gonzalez-Feliciano, A. G.; Sutcliffe, S.; Platz, E. A.; Mucci, L. A.; Ebot, E. M. Association between Trichomonas vaginalis and prostate cancer mortality. *Int J Cancer* **2019**, *144* (10), 2377–2380. DOI: 10.1002/ijc.31885.

(5) Van Gerwen, O. T.; Muzny, C. A. Recent advances in the epidemiology, diagnosis, and management of Trichomonas vaginalis infection. *F1000Res* **2019**, *8*. DOI: 10.12688/f1000research.19972.1.

(6) Zhang, Z.; Li, Y.; Lu, H.; Li, D.; Zhang, R.; Xie, X.; Guo, L.; Hao, L.; Tian, X.; Yang, Z.; et al. A systematic review of the correlation between Trichomonas vaginalis infection and infertility. *Acta Trop* **2022**, *236*, 106693. DOI: 10.1016/j.actatropica.2022.106693.

(7) Flagg, E. W.; Meites, E.; Phillips, C.; Papp, J.; Torrone, E. A. Prevalence of Trichomonas vaginalis Among Civilian, Noninstitutionalized Male and Female Population Aged 14 to 59 Years: United States, 2013 to 2016. *Sex Transm Dis* **2019**, *46* (10), e93–e96. DOI: 10.1097/OLQ.0000000000001013.

(8) Meites, E. Trichomoniasis: the "neglected" sexually transmitted disease. *Infect Dis Clin North Am* **2013**, *27* (4), 755–764. DOI: 10.1016/j.idc.2013.06.003.

(9) Van Gerwen, O. T.; Opsteen, S. A.; Graves, K. J.; Muzny, C. A. Trichomoniasis. *Infect Dis Clin North Am* **2023**, *37* (2), 245–265. DOI: 10.1016/j.idc.2023.02.001.

(10) Muzny, C. A.; Van Gerwen, O. T.; Legendre, D. Secnidazole: a treatment for trichomoniasis in adolescents and adults. *Expert Rev Anti Infect Ther* **2022**, *20* (8), 1067–1076. DOI: 10.1080/14787210.2022.2080656.

(11) Robinson, S. C. Trichomonal Vaginitis Resistant to Metranidazole. *Can Med Assoc J* **1962**, *86* (14), 665.

(12) Steinbuchel, A.; Muller, M. Anaerobic pyruvate metabolism of Tritrichomonas foetus and Trichomonas vaginalis hydrogenosomes. *Mol Biochem Parasitol* **1986**, *20* (1), 57–65. DOI: 10.1016/0166-6851(86)90142-8.

(13) Schneider, R. E.; Brown, M. T.; Shiflett, A. M.; Dyall, S. D.; Hayes, R. D.; Xie, Y.; Loo, J. A.; Johnson, P. J. The Trichomonas vaginalis hydrogenosome proteome is highly reduced relative to mitochondria, yet complex compared with mitosomes. *Int J Parasitol* **2011**, *41* (13-14), 1421–1434. DOI: 10.1016/j.ijpara.2011.10.001.

(14) Rada, P.; Makki, A. R.; Zimorski, V.; Garg, S.; Hampl, V.; Hrdy, I.; Gould, S. B.; Tachezy, J. N-Terminal Presequence-Independent Import of Phosphofructokinase into Hydrogenosomes of Trichomonas vaginalis. *Eukaryot Cell* **2015**, *14* (12), 1264–1275. DOI: 10.1128/EC.00104-15.

(15) Bryan, C. M.; Bhandari, J.; Napuli, A. J.; Leibly, D. J.; Choi, R.; Kelley, A.; Van Voorhis, W. C.; Edwards, T. E.; Stewart, L. J. High-throughput protein production and purification at the Seattle Structural Genomics Center for Infectious Disease. *Acta Crystallogr Sect F Struct Biol Cryst Commun* **2011**, *67* (Pt 9), 1010–1014. DOI: 10.1107/S1744309111018367.

(16) Choi, R.; Kelley, A.; Leibly, D.; Hewitt, S. N.; Napuli, A.; Van Voorhis, W. Immobilized metal-affinity chromatography protein-recovery screening is predictive of crystallographic structure success. *Acta Crystallogr Sect F Struct Biol Cryst Commun* **2011**, *67* (Pt 9), 998–1005. DOI: 10.1107/S1744309111017374.

(17) Serbzhinskiy, D. A.; Clifton, M. C.; Sankaran, B.; Staker, B. L.; Edwards, T. E.; Myler, P. J. Structure of an ADP-ribosylation factor, ARF1, from Entamoeba histolytica bound to Mg(2+)-GDP. *Acta Crystallogr F Struct Biol Commun* **2015**, *71* (Pt 5), 594–599. DOI: 10.1107/S2053230X15004677.

(18) Studier, F. W. Protein production by auto-induction in high density shaking cultures. *Protein Expr Purif* **2005**, *41* (1), 207–234. DOI: 10.1016/j.pep.2005.01.016.

(19) Gorrec, F. The MORPHEUS protein crystallization screen. *J Appl Crystallogr* **2009**, *42* (Pt 6), 1035–1042. DOI: 10.1107/S0021889809042022.

(20) Kabsch, W. Xds. *Acta crystallographica. Section D, Biological crystallography* **2010**, *66* (Pt 2), 125–132. DOI: 10.1107/S0907444909047337.

(21) Collaborative Computational Project, N. The CCP4 suite: programs for protein crystallography. *Acta Cryst.* **1994**, *D50*, 760–763.

(22) Krissinel, E. B.; Winn, M. D.; Ballard, C. C.; Ashton, A. W.; Patel, P.; Potterton, E. A.; McNicholas, S. J.; Cowtan, K. D.; Emsley, P. The new CCP4 Coordinate Library as a toolkit for the design of coordinate-related applications in protein crystallography. *Acta crystallographica. Section D, Biological crystallography* **2004**, *60* (Pt 12 Pt 1), 2250–2255.

(23) Winn, M. D.; Ballard, C. C.; Cowtan, K. D.; Dodson, E. J.; Emsley, P.; Evans, P. R.; Keegan, R. M.; Krissinel, E. B.; Leslie, A. G.; McCoy, A.; et al. Overview of the CCP4 suite and current developments. *Acta crystallographica. Section D, Biological crystallography* **2011**, *67* (Pt 4), 235–242, Research Support, Non-U.S. Gov't. DOI: 10.1107/S0907444910045749.

(24) Agirre, J.; Atanasova, M.; Bagdonas, H.; Ballard, C. B.; Basle, A.; Beilsten-Edmands, J.; Borges, R. J.; Brown, D. G.; Burgos-Marmol, J. J.; Berrisford, J. M.; et al. The CCP4 suite: integrative

software for macromolecular crystallography. *Acta Crystallogr D Struct Biol* **2023**, *79* (Pt 6), 449–461. DOI: 10.1107/S2059798323003595.

(25) Emsley, P.; Lohkamp, B.; Scott, W. G.; Cowtan, K. Features and development of Coot. *Acta Crystallogr D Biol Crystallogr* **2010**, *66* (Pt 4), 486–501. DOI: 10.1107/S0907444910007493.

(26) Adams, P. D.; Afonine, P. V.; Bunkoczi, G.; Chen, V. B.; Davis, I. W.; Echols, N.; Headd, J. J.; Hung, L. W.; Kapral, G. J.; Grosse-Kunstleve, R. W.; et al. PHENIX: a comprehensive Python-based system for macromolecular structure solution. *Acta crystallographica. Section D, Biological crystallography* **2010**, *66* (Pt 2), 213–221. DOI: 10.1107/S0907444909052925.

(27) Liebschner, D.; Afonine, P. V.; Baker, M. L.; Bunkoczi, G.; Chen, V. B.; Croll, T. I.; Hintze, B.; Hung, L. W.; Jain, S.; McCoy, A. J.; et al. Macromolecular structure determination using X-rays, neutrons and electrons: recent developments in Phenix. *Acta Crystallogr D Struct Biol* **2019**, *75* (Pt 10), 861–877. DOI: 10.1107/S2059798319011471.

(28) Williams, C. J.; Headd, J. J.; Moriarty, N. W.; Prisant, M. G.; Videau, L. L.; Deis, L. N.; Verma, V.; Keedy, D. A.; Hintze, B. J.; Chen, V. B.; et al. MolProbity: More and better reference data for improved all-atom structure validation. *Protein Sci* **2018**, *27* (1), 293–315. DOI: 10.1002/pro.3330.

(29) Wu, D.; Piszczek, G. Standard protocol for mass photometry experiments. *Eur Biophys J* **2021**, *50* (3-4), 403–409. DOI: 10.1007/s00249-021-01513-9.

(30) Young, G.; Hundt, N.; Cole, D.; Fineberg, A.; Andrecka, J.; Tyler, A.; Olerinyova, A.; Ansari, A.; Marklund, E. G.; Collier, M. P.; et al. Quantitative mass imaging of single biological macromolecules. *Science* **2018**, *360* (6387), 423–427. DOI: 10.1126/science.aar5839.

(31) Krissinel, E. Stock-based detection of protein oligomeric states in jsPISA. *Nucleic Acids Res* **2015**, *43* (W1), W314–319. DOI: 10.1093/nar/gkv314.

(32) Mertens, E.; Van Schaftingen, E.; Muller, M. Presence of a fructose-2,6-bisphosphate-insensitive pyrophosphate: fructose-6-phosphate phosphotransferase in the anaerobic protozoa Tritrichomonas foetus, Trichomonas vaginalis and Isotricha prostoma. *Mol Biochem Parasitol* **1989**, *37* (2), 183–190. DOI: 10.1016/0166-6851(89)90150-3.

(33) Reeves, R. E.; Serrano, R.; South, D. J. 6-phosphofructokinase (pyrophosphate). Properties of the enzyme from Entamoeba histolytica and its reaction mechanism. *J Biol Chem* **1976**, *251* (10), 2958–2962.

(34) Bertagnolli, B. L.; Cook, P. F. Lanthanide pyrophosphates as substrates for the pyrophosphate-dependent phosphofructokinases from Propionibacterium freudenreichii and Phaseolus aureus: evidence for a second metal ion required for reaction. *Biochemistry* **1994**, *33* (7), 1663–1667. DOI: 10.1021/bi00173a007.

(35) Laskowski, R. A.; Swindells, M. B. LigPlot+: multiple ligand-protein interaction diagrams for drug discovery. *J Chem Inf Model* **2011**, *51* (10), 2778–2786. DOI: 10.1021/ci200227u.

(36) Wallace, A. C.; Laskowski, R. A.; Thornton, J. M. LIGPLOT: a program to generate schematic diagrams of protein-ligand interactions. *Protein Eng* **1995**, *8* (2), 127–134.

(37) Gouet, P.; Robert, X.; Courcelle, E. ESPript/ENDscript: Extracting and rendering sequence and 3D information from atomic structures of proteins. *Nucleic Acids Res* **2003**, *31* (13), 3320–3323.

(38) Robert, X.; Gouet, P. Deciphering key features in protein structures with the new ENDscript server. *Nucleic Acids Res* **2014**, *42* (Web Server issue), W320–324. DOI: 10.1093/nar/gku316.

(39) Moore, S. A.; Ronimus, R. S.; Roberson, R. S.; Morgan, H. W. The structure of a pyrophosphate-dependent phosphofructokinase from the Lyme disease spirochete Borrelia burgdorferi. *Structure* **2002**, *10* (5), 659–671. DOI: 10.1016/s0969-2126(02)00760-8.

(40) Holm, L. Dali server: structural unification of protein families. *Nucleic Acids Research* **2022**, *50* (W1), W210–W215. DOI: 10.1093/nar/gkac387 (accessed 1/10/2026).

(41) McNae, I. W.; Kinkead, J.; Malik, D.; Yen, L. H.; Walker, M. K.; Swain, C.; Webster, S. P.; Gray, N.; Fernandes, P. M.; Myburgh, E.; et al. Fast acting allosteric phosphofructokinase inhibitors block trypanosome glycolysis and cure acute African trypanosomiasis in mice. *Nat Commun* **2021**, *12* (1), 1052. DOI: 10.1038/s41467-021-21273-6.

(42) Mosser, R.; Reddy, M. C.; Bruning, J. B.; Sacchettini, J. C.; Reinhart, G. D. Redefining the role of the quaternary shift in Bacillus stearothermophilus phosphofructokinase. *Biochemistry* **2013**, *52* (32), 5421–5429. DOI: 10.1021/bi4002503.

(43) Compton, J. A.; Patrick, W. M. The more we learn, the more diverse it gets: structures, functions and evolution in the Phosphofructokinase Superfamily. *Biochem J* **2025**, *482* (9), 467–483. DOI: 10.1042/BCJ20253024.

(44) Gouet, P.; Courcelle, E.; Stuart, D. I.; Metoz, F. ESPript: analysis of multiple sequence alignments in PostScript. *Bioinformatics* **1999**, *15* (4), 305–308.

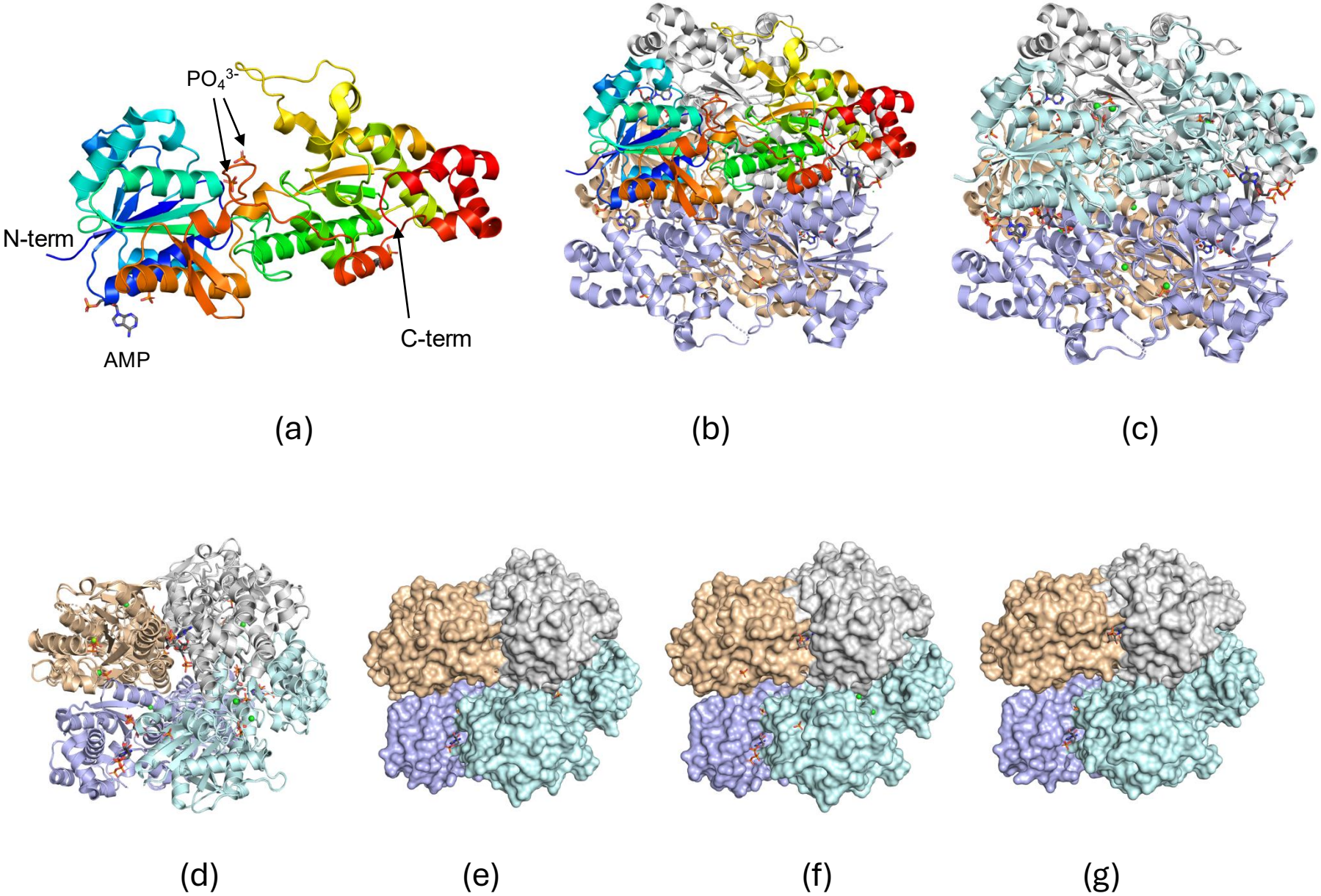

Figure 1

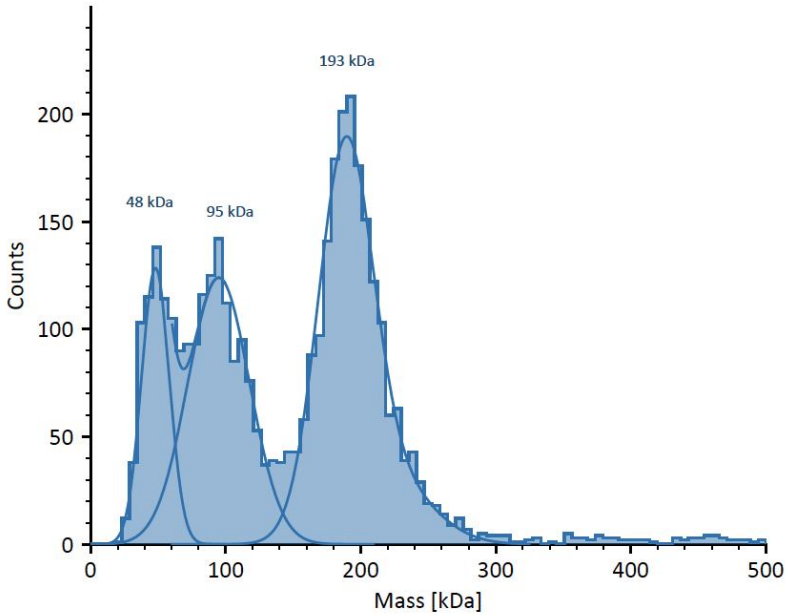
193 kDa
48 kDa
95 kDa
Counts
Mass [kDa]
0
50
100
150
200
0
100
200
300
400
500

(a)

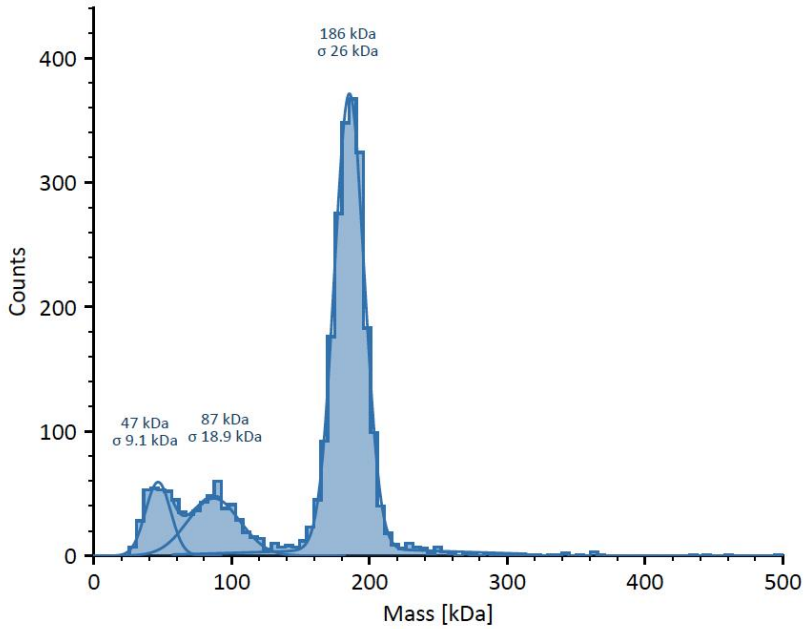
186 kDa
σ 26 kDa
47 kDa
σ 9.1 kDa
87 kDa
σ 18.9 kDa
Counts
Mass [kDa]
0
100
200
300
400
0
100
200
300
400
500

(b)

Figure 2

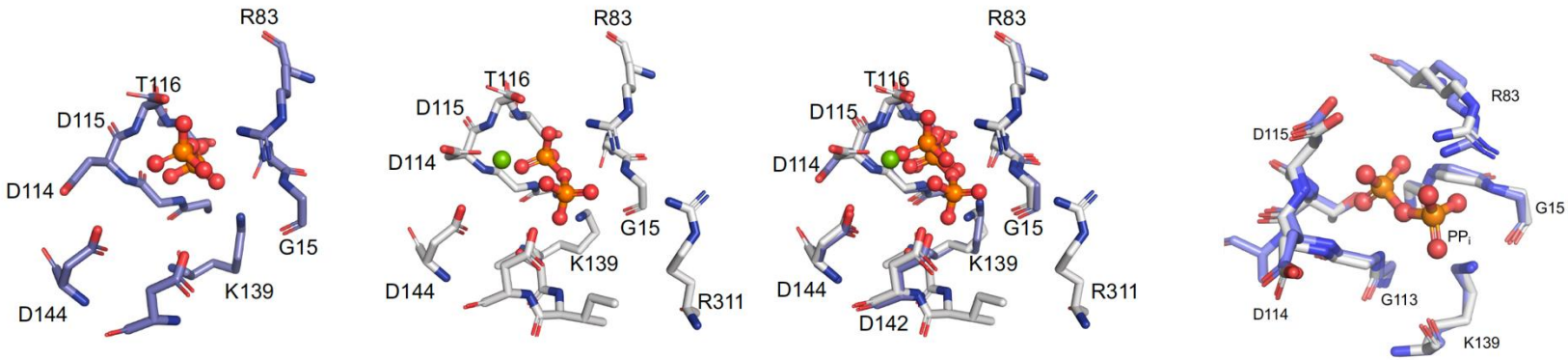

9MDT PPi

(a)

9MED 1MgPPi2-

(b)

9MED, 9MDT

(c)

(d)

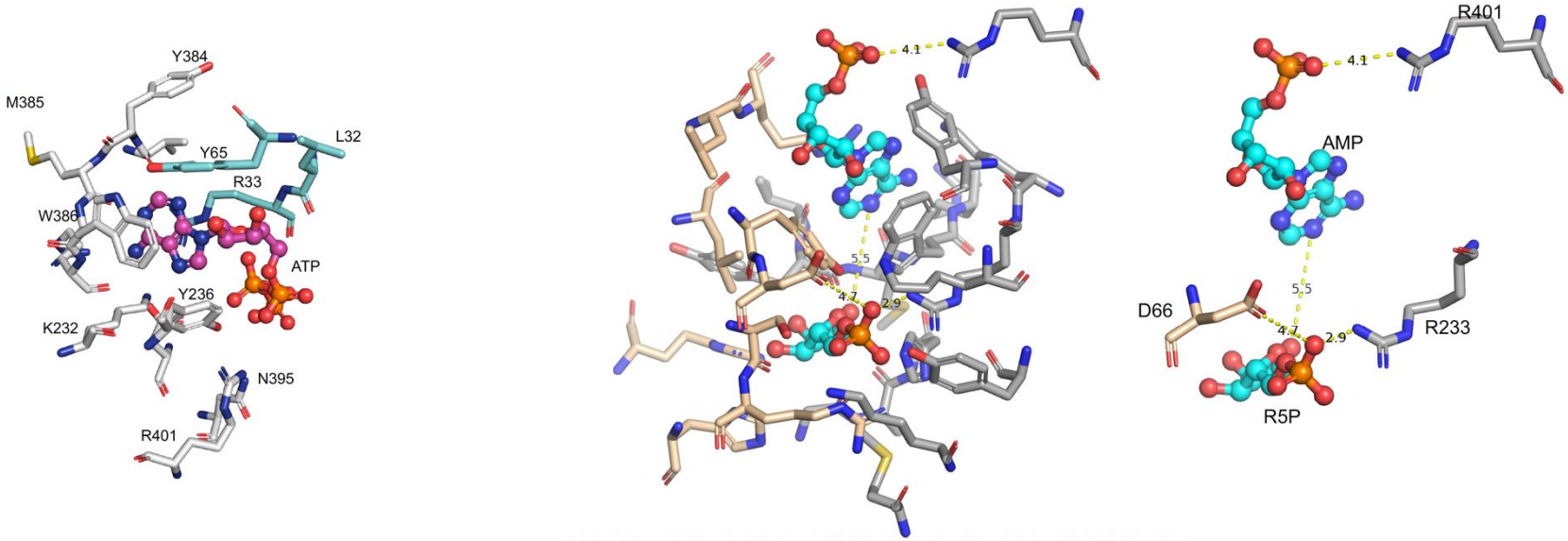

(e)

Figure 3

(f)

(g)

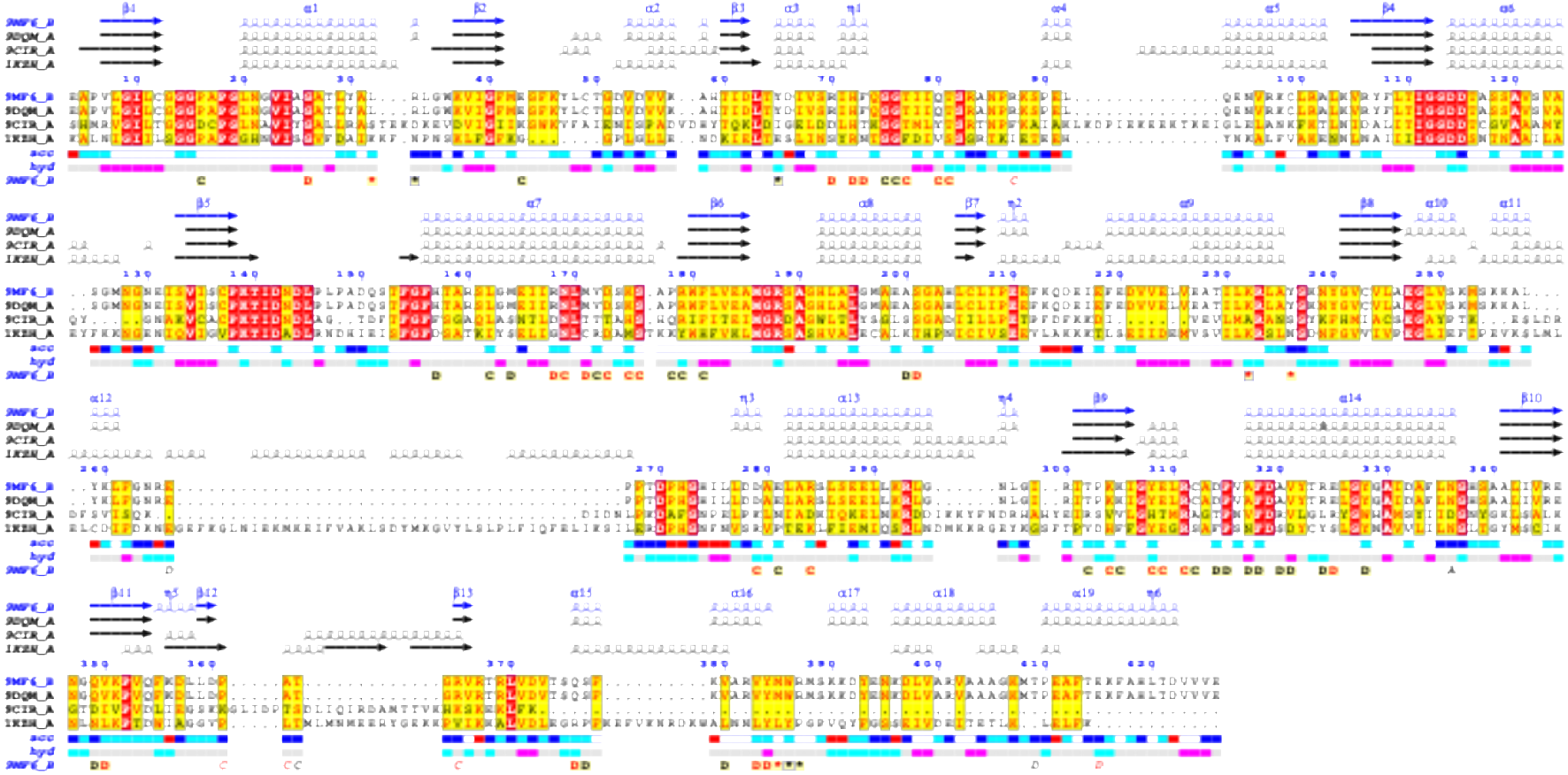

Supported bound ligand AMP*

Figure 4

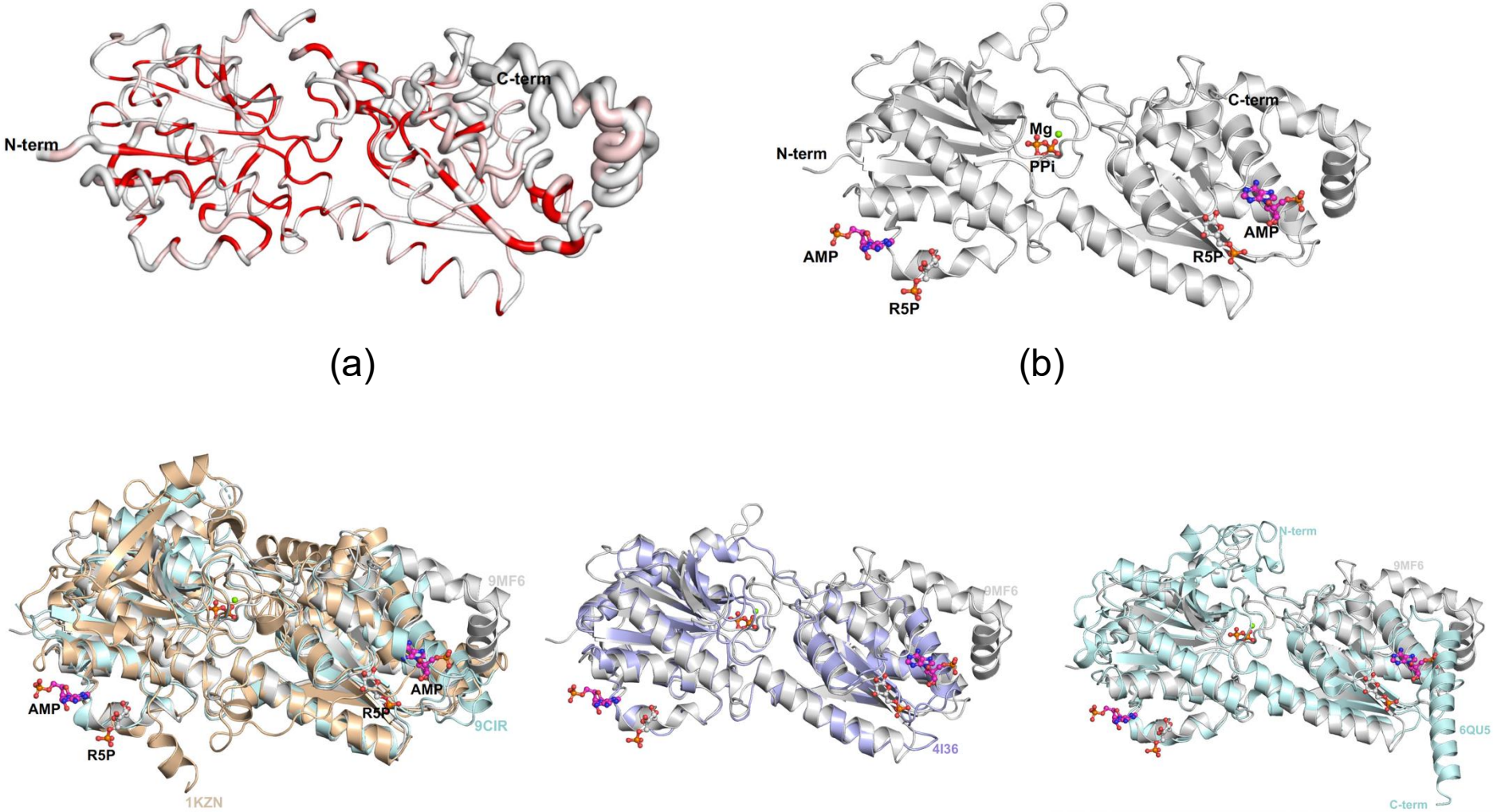
N-term
C-term
(a)
N-term
Mg
PPi
C-term
AMP
R5P
AMP
R5P
(b)
9MF6
AMP
R5P
AMP
9CIR
R5P
1KZN
(c)
9MF6
4I36
(d)
N-term
9MF6
6QU5
C-term
(e)

Figure 5